

Article

An Impact of the Discrete Representation of the Bubble Size Distribution Function on the Flow Structure in a Bubble Column Reactor

Alexander Chernyshev ^{1,*} , Alexander Schmidt ¹  and Veronica Chernysheva ²

¹ Computational Physics Laboratory, Ioffe Institute, Politekhnikeskaya Str. 26, 194021 St. Petersburg, Russia

² Department of Energy, Peter the Great St. Petersburg Polytechnic University, Politekhnikeskaya Str. 29, 195251 St. Petersburg, Russia

* Correspondence: alexander.tchernyshev@mail.ioffe.ru

Abstract: The purpose of the present study is to analyze the effect of different discrete representations of the continuous bubble size distribution function on the flow structure in a bubble column reactor. Poly- and monodisperse media were considered, such that the mathematical expectation of the bubble size in the polydisperse case was equal to the bubble size in the monodisperse case at the same volumetric bubble contents. For these computations the normalized variances of the velocity profiles of the carrier and the disperse phases, the volume fraction of the disperse phase, and the specific area of the interfacial surface were determined. The normalized variances were calculated from a reference scenario with a detailed resolution of the bubble size distribution function with ten bubble classes. It was shown that with increase of the average bubble sizes mono- and polydisperse approaches provide converging solutions. A modified hybrid discretization of the bubble size distribution function with four classes of bubbles was shown to predict the flow structure with normalized variance less than 5% over the entire computational domain for all monitored parameters.

Keywords: bubble column reactor; bubbly flow; polydisperse media; numerical simulation; Euler–Euler approach; discrete bubble size distribution function



Citation: Chernyshev, A.; Schmidt, A.; Chernysheva, V. An Impact of the Discrete Representation of the Bubble Size Distribution Function on the Flow Structure in a Bubble Column Reactor. *Water* **2023**, *15*, 778. <https://doi.org/10.3390/w15040778>

Academic Editor: Arthur Mynett

Received: 27 January 2023

Revised: 13 February 2023

Accepted: 14 February 2023

Published: 16 February 2023



Copyright: © 2023 by the authors. Licensee MDPI, Basel, Switzerland. This article is an open access article distributed under the terms and conditions of the Creative Commons Attribution (CC BY) license (<https://creativecommons.org/licenses/by/4.0/>).

1. Introduction

Ascending bubble flows with the gravity force as the main driver are a common feature of many natural and technological processes. Typical industrial applications of such flows are bubble column reactors (BCRs). These apparatus are used in many areas of human activity, such as water treatment and purification [1], greenhouse gas elimination [2], hydrogen and biofuel synthesis [3,4], or production of biochemical substances [5]. All of the above shows that studies of the processes occurring in the BCRs are of great importance.

As a rule, the flows in the BCR are polydisperse; this circumstance plays an important role in the formation of both the global structure of the flows [6,7] and the local properties of the working media of reactors [4,8].

The description of the bubble size distribution (BSD) in the framework of the polydisperse Euler–Euler approach can be implemented in various ways. The simplest one is similar to the monodisperse description, but the bubbles have the same size only locally; herewith they can vary in space. The local size of the bubbles is taken to be equal to the Sauter mean diameter [9], which ensures that the total bubble surface is preserved, and is important in problems with intensive interphase mass transfer. At low relative velocities this approach is sufficient. However, at phase velocity nonequilibrium, averaging the bubble diameter results in errors in the calculation of interphase forces, which in turn affects the overall flow pattern.

A detailed description of polydispersity within the Euler–Euler approach can be provided by the Population Balance Model (PBM) [4,10] with a population balance equation.

This model makes it possible to describe the change in the spectrum of bubble sizes at each spatial point but the computational algorithm becomes noticeably more complicated because of the integral–differential nature of the equation.

Another approach which is a subclass of the PBM is based on the introduction of a set of classes of monodisperse bubbles that differ in size (the Multiple Size Group or MUSIG model) [11]. The original model has the same velocity for each bubble class and is called homogeneous MUSIG, while its variant with separate velocity for each class is called the inhomogeneous or heterogeneous MUSIG model [12]. A fixed number of classes and ranges of bubble sizes in the classes are chosen to include all possible bubbles. Sets of the conservation equations are written for each class. Such an approach provides a unified description of the working medium. However, this approach is also quite resource-demanding due to the need to solve additional sets of nonlinear equations.

Due to the significant increase in computational resources required, it seems reasonable to assess the influence of the parameters of the discrete representation of the (BSD) function on the flow structure for the regimes where polydispersity is the determining factor.

There are a number of papers dealing with the discretization parameters of the BSD. An unsteady simulation of the BCR was performed in [13] with only two classes for the 13 mm/s surface velocity case, while a monodisperse approach was sufficient for the 3 mm/s surface velocity. The two classes for the 13 mm/s case were chosen to resolve a change in the sign of the lateral lift force at 6 mm bubble diameter. There are other investigations [14,15] which show that for gas surface velocities below 5 mm/s the monodisperse approach is sufficient.

Numerical simulations of the BSD have been performed in [7,16]. With 17 classes of bubbles it was shown [7] that good prediction can be obtained for most of the bubble size range [0.5 mm, 16.5 mm], while the probability of small bubbles was underestimated by the model. Reducing the number of classes [16] from 17 to 14 provides better correlation with experimental data.

A detailed investigation of the effect of the number of bubble classes was carried out in [17]. It was shown that seven classes of bubbles were sufficient for the detailed description of the flow in the BCR in terms of liquid velocity, bubble velocity and bubble volume fraction. However, for the prediction of the interfacial area, 15 classes were selected in the computations. In the subsequent study [18] it was shown that the heterogeneous MUSIG outperformed the original homogeneous version. The same results were obtained in [19] for the simplified heterogeneous MUSIG model with algebraic equations for bubble slip velocities with 13 classes of bubbles for the bubble size range [1 mm, 25 mm].

It should be noted that all of these studies deal with the uniform BSD and it is not clear how the bubble swarm behaves with bubble sizes ranging from fractions of a millimeter to a few millimeters.

The paper presents the results of a numerical study of the dynamics of poly- and monodisperse flows in a column-type bubble reactor. The mathematical expectation of the bubble size for a polydisperse medium was assumed to be equal to the bubble size in a monodisperse medium. Bubbles with characteristic sizes in the range $d_b = 0.25\text{--}1.0$ mm are considered; the volume content of the dispersed phase at the inlet boundary was the same in all cases and was equal to 0.0037. Different discretization parameters of the BSD function were chosen to estimate their influence on the flow structure in the BCR.

According to the results of the numerical simulation, the fields of phase velocities, bubble volume fraction and the interfacial area, which influence the intensity of interphase processes, were analyzed. On the basis of the obtained data, an optimal number of classes, as well as the discretization parameters of the BSD function, were chosen in order to obtain a consistent solution in the whole range of the input parameters considered.

2. Mathematical Model

2.1. Basic Assumptions of the Model

A mathematical model of the flow of a polydisperse bubble medium in a bubble column reactor is presented. The model is based on the Euler–Euler approach to the description of multiphase flows (see, for example, [20]). Within the framework of this approach, each phase is considered as a continuum occupying the entire volume, at each point of which the volume fraction of the phase α is specified. In this case, the densities of each of the phases are calculated as $\alpha \cdot \rho_0$, where ρ_0 is the density of the substance of the corresponding phase. In addition to the description of the polydispersity and the interaction of the bubbles (subscript b) and the carrier phase (subscript l), attention is paid to the analysis of the effect of turbulence on the two-phase flow.

In this study, flows are characterized by values of the dispersed phase volume fraction less than 0.01, which allows bubble–bubble interactions to be neglected.

2.2. Description of Polydispersity of Bubbly Medium

The description of the polydispersity of the working medium is carried out in the framework of the multiclass heterogeneous model of the BSD, which takes into account the different speeds of each bubble class (the heterogeneous MUSIG model, [12]). The BSD is approximated by a piecewise constant function describing N bubble classes. Each of the classes is characterized by the constant bubble diameter d_{ib} , the volume fraction α_{ib} and the bubble number density n_{ib} , where i is the class number. These quantities are related to each other as $d_{ib} = ((6\alpha_{ib})/(\pi n_{ib}))^{1/3}$. Then the volume fraction of the liquid can be represented as follows:

$$\alpha_l = 1 - \sum_{i=1}^N \alpha_{ib}. \quad (1)$$

The initial BSD corresponds to the experimental data and can be expressed by the log-normal distribution for the bubble number density [21]:

$$F(n_b) = \frac{1}{d_b \sigma \sqrt{2\pi}} \cdot \exp\left(\frac{-[\ln(d_b) - \mu]^2}{2\sigma^2}\right), \quad (2)$$

where d_b is the bubble diameter, and μ and σ are the mathematical expectation and standard deviation with respect to $\ln(d_b)$. The mathematical expectation M and the standard deviation D with respect to d_b are determined by the formulas:

$$M = \exp(\mu + 0.5 \cdot \sigma^2), \quad D = M \cdot \sqrt{[\exp(\sigma^2) - 1]}. \quad (3)$$

In Equation (3), the value M corresponds to the most probable bubble for a given distribution and will be referred to below as the characteristic bubble size. The monodisperse case is obtained by integrating over the entire interval of bubble sizes, producing a single class of bubbles with a size equal to the most probable bubble size. In this sense, the monodisperse approach can be treated as a polydisperse approach with only one class of bubbles.

The equations of conservation of mass, momentum and number density of the bubbles are formulated for each class.

2.3. Governing Equations

In the framework of the Euler–Euler approach the Navier–Stokes equations, accounting for the N bubble classes, can be written as follows:

$$\begin{aligned}
\frac{\partial \alpha_{ib} \rho_{ib}^0}{\partial t} + \text{div}(\alpha_{ib} \rho_{ib}^0 \mathbf{V}_{ib}) &= D_{ib}, \\
\frac{\partial \alpha_{ib} \rho_{ib}^0 \mathbf{V}_{ib}}{\partial t} + \text{div}(\alpha_{ib} \rho_{ib}^0 \mathbf{V}_{ib} \mathbf{V}_{ib} + p \mathbf{E}) &= S_{ib}, \\
\frac{\partial \alpha_l \rho_l^0}{\partial t} + \text{div}(\alpha_l \rho_l^0 \mathbf{V}_l) &= 0, \\
\frac{\partial \alpha_l \rho_l^0 \mathbf{V}_l}{\partial t} + \text{div}(\alpha_l \rho_l^0 \mathbf{V}_l \mathbf{V}_l + p \mathbf{E} - \boldsymbol{\tau}) &= S_l.
\end{aligned} \tag{4}$$

The following notation is used: \mathbf{V} is the velocity vector, p is the pressure, \mathbf{E} is the unity tensor, S is the source term responsible for the interphase momentum transport, D is the source term responsible for the bubble dispersion due to turbulence and $\boldsymbol{\tau}$ is the strain rate tensor with its components expressed as:

$$\tau_{mn} = 2 \cdot \mu_{eff} \cdot S_{mn}, \quad S_{mn} = \frac{1}{2} \left(\frac{\partial v_m}{\partial x_n} + \frac{\partial v_n}{\partial x_m} \right), \quad \mu_{eff} = \mu_{lam} + \mu_{turb} + \mu_{BIT}, \tag{5}$$

where μ_{eff} is the effective dynamic viscosity, equal to sum of the dynamic viscosity of the medium μ_{lam} , the turbulent viscosity μ_{turb} and an additional member, responsible for turbulence modification due to presence of bubbles μ_{BIT} .

The density of the gas inside the bubbles ρ_{ib}^0 depends on both the external pressure of the carrier medium and on the pressure created by the surface tension, and can be expressed as follows:

$$\rho_{ib}^0 = \frac{p + 2\Sigma/R_{ib}}{\Re_b T_0}, \tag{6}$$

where Σ is the surface tension (assumed to be equal to 0.072 H/m), R_{ib} is the bubble radius for the i th class, T_0 is the ambient temperature and \Re_b is the specific gas constant.

The set of Equation (4) is supplemented by the conservation equation for the bubble number density for each class i :

$$\frac{\partial n_{ib}}{\partial t} + \text{div}(n_{ib} \mathbf{V}_{ib}) = D_{in}. \tag{7}$$

2.4. Interphase Momentum Exchange

The details of the interphase momentum exchange processes are discussed below. Corresponding source terms in the governing equations include: the buoyancy force, the drag (Stokes) force, the lift (Saffman) force, the virtual mass force and the wall lubrication force:

$$S_{ib} = \mathbf{F}_{iB} + \mathbf{F}_{iD} + \mathbf{F}_{iL} + \mathbf{F}_{iWL} + \mathbf{F}_{iVM}, \quad S_l = - \sum_{i=1}^N (\mathbf{F}_{iD} + \mathbf{F}_{iL} + \mathbf{F}_{iWL} + \mathbf{F}_{iVM}). \tag{8}$$

2.4.1. Buoyancy Force

The buoyancy force is the main driver of flow development in the column and is expressed as the difference between the Archimedean and gravitational forces:

$$\mathbf{F}_{iB} = \alpha_{ib} \cdot (\rho_{ib} - \rho_l) \cdot \mathbf{g}. \tag{9}$$

2.4.2. Drag Force

The expression for the Stokes drag force acting on bubbles of class i can be written in the following form:

$$\mathbf{F}_{iD} = \frac{3}{8} \cdot \frac{\rho_l}{R_{ib}} \alpha_{ib} C_{iD} \mathbf{V}_{irel} |\mathbf{V}_{irel}|, \quad \mathbf{V}_{irel} = \mathbf{V}_l - \mathbf{V}_{ib}. \quad (10)$$

In the general case, when the Reynolds number of the relative motion of the phases $Re_{ip} = (\rho_l V_{irel} d_{ib}) / \mu_{lam}$ cannot be considered small, it is necessary to introduce a correction function f_{ip} for the Stokes drag coefficient, which takes into account the inertia of the flow around the bubbles, their possible asymmetry, flows in the bubbles, etc. Thus, the drag coefficient can be written as $C_{iD} = 24 \cdot f_{ip} / Re_{ip}$. During the calculations, several options were considered to determine the function f_{ip} . In Ref. [22], the following expression for the correction function is proposed, based on experimental data:

$$f_{ip} = \begin{cases} 2/3, & Re_{ip} < 1.5 \\ 0.6208 Re_{ip}^{0.22}, & 1.5 < Re_{ip} < 80 \\ 2 - 4.41 Re_{ip}^{-0.5} + 7.75 \cdot 10^{-17} Re_{ip}^{5.756}, & 80 < Re_{ip} < 1500 \\ 0.10875 Re_{ip}, & Re_{ip} > 1500 \end{cases} \quad (11)$$

This expression describes the dynamics of small bubbles, but does not take into account the possible deformation of the interfaces and the loss of sphericity.

The shape of the bubble may be different from spherical if the pressure changes significantly on scales of bubble size. Assuming that the main reason for the pressure variation is gravity, then the effect of the pressure gradient is determined by the Eötvös number $Eo_i = g(\rho_l - \rho_{ib})d_{ib}^2 / \Sigma$, which is the ratio of the hydrostatic pressure of a liquid column whose height is equal to the size of the bubble to the pressure produced by the surface tension force. At $Eo < 1$ the bubble remains spherical, at $Eo > 1$ the bubble loses its sphericity, acquiring at the initial stage the shape of an ellipsoid. In Ref. [23], a correlation was proposed for the drag coefficient C_{iD} based on the Reynolds numbers Re_{ip} and Eo_i :

$$C_{iD} = \sqrt{C_D(Re_{ip})^2 + C_D(Eo_i)^2}$$

$$C_D(Re_{ip}) = \frac{16}{Re_{ip}} \left(1 + \frac{2}{1 + 16/Re_{ip} + 3.315/\sqrt{Re_{ip}}} \right) \quad (12)$$

$$C_D(Eo_i) = 4 \cdot Eo_i / (Eo_i + 9.5), \quad Eo_i < 5$$

In this study, expression (12) for the drag force was used.

2.4.3. Lift Force

The Saffman force occurs when particles move in a stream with significant velocity gradients. The resulting force is normal to the particle relative velocity vector. Although the value of this force is usually much smaller than the Stokes force, it can have a noticeable effect on the structure of the flow and the distribution of bubbles.

The expression for the Saffman force was initially obtained under a number of assumptions, in particular, for the case of low Reynolds numbers of relative motion (Stokes flow), which are not applicable to the problems considered.

For the range of flow parameters of practical interest, the formula proposed in [24] was chosen. Here the expression for the Saffman force can be written as:

$$\mathbf{F}_{iL} = C_{iL} \alpha_{ib} \rho_l \mathbf{V}_{irel} \times \text{rot} \mathbf{V}_l. \quad (13)$$

The coefficient C_{iL} is often taken to be constant, ranged in 0.1–0.5, depending on the type of problem.

Based on a large set of experimental data on the ascent of a single bubble in a liquid layer with a transverse linear velocity gradient, the following expression for the coefficient C_{iL} was proposed in [25]:

$$C_{iL} = \min[0.288 \tanh(0.121 \operatorname{Re}_{ip}), f(\operatorname{Eo}_i)], \operatorname{Eo}_i < 4, \quad (14)$$

$$f(\operatorname{Eo}_i) = 0.00105 \operatorname{Eo}_i^3 - 0.0159 \operatorname{Eo}_i^2 - 0.0204 \operatorname{Eo}_i + 0.474.$$

When calculating the Saffman transverse force, expression (14) was used in this study.

2.4.4. Virtual Mass Force

It is well known that the effect of added masses in bubble flows plays an important role. This effect is associated with an increase of the bubble inertia due to the inclusion of the ambient liquid in relative motion. The expression for the added mass force can be written as:

$$\mathbf{F}_{iVM} = 0.5\alpha_{ib}\rho_l \left(\frac{D_b \mathbf{V}_{ib}}{Dt} - \frac{D_l \mathbf{V}_l}{Dt} \right). \quad (15)$$

2.4.5. Wall Lubrication Force

Near the channel walls, the flow is characterized by a significant gradient of the velocity and asymmetry in the flow around a separate bubble, resulting in repulsion of the bubble from the wall. This effect can be important in the formation of the bubble flow structure and can lead to flow stratification. The expression for the wall force can be written as follows [12]:

$$\mathbf{F}_{iWL} = -C_{iWL}\alpha_{ib}\rho_l [\mathbf{V}_{irel} - (\mathbf{V}_{ib} \cdot \mathbf{n}_W) \cdot \mathbf{n}_W]^2 \cdot \mathbf{n}_W. \quad (16)$$

Here \mathbf{n}_W is the normal to the nearest wall.

Coefficient C_{iWL} is calculated using the following formula:

$$-C_{iWL} = 0.47 \cdot \max \left\{ 0, \frac{1}{6.3} \cdot \frac{[1 - y_W / (10 d_{ib})]}{y_W \cdot [y_W / (10 d_{ib})]^{0.7}} \right\}. \quad (17)$$

Here y_W is the distance to the nearest wall.

2.5. Turbulence

Typical flows in the BCR are turbulent. The presence of a dispersed phase can lead to both the generation and dissipation of turbulence, depending on the flow parameters. An analysis of the influence of these processes on the flow structure in the BCR is of a great interest. In this paper, the $k - \omega$ SST turbulence model [26] is implemented with additional source terms describing the generation of turbulence due to the relative motion of the bubbles and the carrier phase:

$$\begin{aligned} \frac{\partial \rho_l k}{\partial t} + \operatorname{div}(\rho_l \mathbf{V}_l k) &= \tilde{\mathbf{P}} - \beta^* \rho_l \omega k + \operatorname{div}[(\mu_{lam} + \sigma_k \mu_{turb}) \operatorname{grad}(k)] + S_{bk}, \\ \frac{\partial \rho_l \omega}{\partial t} + \operatorname{div}(\rho_l \mathbf{V}_l \omega) &= \alpha_{k\omega} \frac{\rho_l}{\mu_{turb}} \tilde{\mathbf{P}} - \beta \rho_l \omega^2 + \operatorname{div}[(\mu_{lam} + \sigma_\omega \mu_{turb}) \operatorname{grad}(\omega)] + \\ &\quad 2(1 - F_1) \rho_l \sigma_{\omega 2} \cdot \frac{1}{\omega} \frac{\partial k}{\partial x_j} \frac{\partial \omega}{\partial x_j} + S_{b\omega}, \\ \mu_{turb} &= \frac{\rho_l a_1 k}{\max(a_1 \omega, \Omega F_2)}. \end{aligned} \quad (18)$$

Here k is the turbulence kinetic energy and ω is the specific dissipation rate. All constants and closing relations are taken from [26].

2.5.1. Turbulence Generation and Dissipation by Bubbles

The modified model of Troshko and Hassan [27], originally developed for the $k - \epsilon$ turbulence model, is used here to account for the effect of the generation of turbulence by the bubbles. Corresponding source terms in the equations for k and ω can be written as:

$$S_{bk} = \frac{3}{8} \frac{C_{iD}}{R_{ib}} \alpha_{ib} \rho_l |\mathbf{V}_{irel}|^3, S_{b\omega} = 0.8 \frac{k}{\mu_{turb}} S_{bk}, \quad (19)$$

An additional term responsible for the effect of turbulence generation in the expression for the effective viscosity (5) is calculated based on Sato model [28]:

$$\mu_{BIT} = 1.2 \cdot \alpha_{ib} \rho_l R_{ib} |\mathbf{V}_{irel}|. \quad (20)$$

2.5.2. Bubble Path Dispersion

The dispersion of bubbles due to turbulent velocity fluctuations in the carrier phase is accounted for by introducing an additional diffusion term in the equations for the volume fraction of bubbles and the bubble number density [29]:

$$D_{i\alpha} = \frac{1}{Sc} \text{div} \left(\frac{\mu_{eff}}{\rho_l} \text{grad}(\alpha_{ib}) \right), D_{in} = \frac{1}{Sc} \text{div} \left(\frac{\mu_{eff}}{\rho_l} \text{grad}(n_{ib}) \right). \quad (21)$$

Here Sc is the Schmidt number with $Sc = 0.83$; the value is based on the comparison with experimental data of other authors [29,30].

Thus, the set of the conservation equations and closing relations for flows in the BCR are formulated.

2.6. Numerical Method

An algorithm and a computer code are developed for the numerical implementation of the model described above.

The algorithm is based on a common approach using the finite volume method and unstructured grids. Special attention is paid to the discretization of the convection and diffusion terms, both of which are discretized with second-order accuracy. The convection term is discretized using a second-order upwind discretization that satisfies the total variation diminishing (TVD) criterion. Three types of TVD limiters were tested: minmod, vanLeer and superbee. The minmod limiter was used in the computations due to the high stability of the resulting computational scheme.

The source terms resulting from the interphase interactions usually have nonlinear components which can affect the stability of the solution. To overcome this effect, a linearization of implicitly calculated source terms was introduced, especially for the drag force.

The coupling of the pressure and velocity fields was performed by the modified SIMPLE (Phase Coupled-SIMPLE) algorithm, taking into account the effects of multiphase. The PC-SIMPLE includes not only the major liquid phase fluxes in the calculation of pressure corrections but also the minor fluxes of the bubble phase. Rhie–Chow interpolation is used to avoid non-physical oscillations when updating the pressure and velocity fields.

The resulting discretized equations are solved by iterative methods such as Gauss–Zeidel with successive over-relaxations. The pressure correction equation is solved by the preconditioned conjugate gradient method with incomplete zero-filling Cholesky decomposition as preconditioner.

A detailed description of the basis of the numerical method can be found in [31].

The developed mathematical model, numerical methods and computer code have been extensively tested on the flows under study [20,32,33].

3. Problem Statement

3.1. Simulation Domain and Conditions

Since the main goal of this study is to analyze the effects of the description of the polydispersity of the working medium of the BCR, a series of calculations were carried out using various parameters of the piecewise constant representation of the BSD. Different numbers of classes N and different characteristic sizes of bubbles M were considered at their constant flow rate. Flows in axisymmetric BCRs due to Archimedes' force are considered using a simplified

axisymmetric formulation. In Refs. [34,35] it was shown that such an approach allows the main features of the flows under study to be captured.

The analysis is performed for flows in a vertical cylindrical BCR with a coaxial aerator at the bottom and the top open.

Figure 1 shows a schematic diagram of an axisymmetric BCR; reactor diameter is $D = 0.07$ m and reactor height is $H = 0.65$ m. The carrier phase is water. The disperse phase, in the form of polydisperse gas bubbles, enters the column through a coaxial axisymmetric bottom mounted aerator ($d = 0.05$ m).

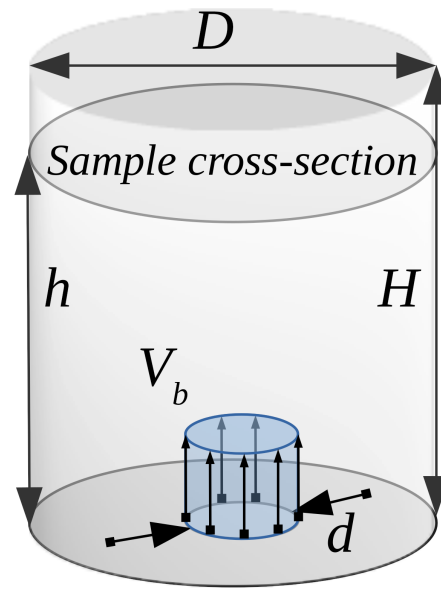


Figure 1. Schematics of a bubble column reactor.

A cross-section at a height of $h = 0.48$ m, depicted in the scheme, is used as a reference cross-section for the presentation of flow parameters.

Normal conditions for ambient gas at the free surface are assumed.

Simulations were carried out on a mesh of 50 cells along the radial coordinate and 90 cells along the axial coordinate, with the mesh denser toward the solid boundaries to provide detailed boundary layer resolution to meet both multiphase and turbulence requirements. Independent mesh sensitivity studies were performed and the presented mesh was selected as adequate. The time step Δt was chosen equal to 10^{-2} s with a normalized convergence criterion of 10^{-6} for each independent variable.

3.2. A Discrete Approximation of the BSD Function

The initial BSD can be described by the lognormal function (2). To determine the most efficient variant of the piecewise constant approximation of this function, three sets of approximations are used, denoted by **R1**, **R2** and **R3**. The entire interval of bubble size variation is replaced by the range $[d_{min}, d_{max}]$, where $d_{min} = \exp(\mu - 3\sigma)$, $d_{max} = \exp(\mu + 3\sigma)$, which corresponds to 99.7% of all bubbles. The **R1** distribution approximation is uniform with respect to the variable d_b in the range $[d_{min}, d_{max}]$; the entire range is divided into N classes, each class having the same width with respect to d_b . The **R2** distribution approximation is uniform with respect to the variable $\ln(d_b)$; the range $[\ln(d_{min}), \ln(d_{max})]$ is divided into N classes, the width of each class with respect to $\ln(d_b)$ is the same. The **R3** approximation is a hybrid **R2–R1**: the first $N/2$ classes are uniformly distributed with respect to the variable $\ln(d_b)$ in the range $[\ln(d_{min}), \mu]$; the subsequent $N/2$ classes are uniformly distributed with respect to the variable d_b in the range $[\exp(\mu), d_{max}]$.

The distribution approximation of type **R1** is used for validation purposes. A set of different numbers of classes is used with $N = [1 \dots 10]$, covering a range from a monodisperse

approach to a detailed polydisperse one. The validation is performed for the characteristic bubble size $M = 0.5$ mm.

The lognormal distributions under consideration correspond to four characteristic bubble sizes M : 0.25 mm, 0.375 mm, 0.5 mm and 1.0 mm. Five combinations of the number of classes and distribution approximation options are introduced: ($N = 1$, **R1**), which corresponds to monodisperse bubbles, ($N = 4$, **R3**), which corresponds to a compact economic distribution, ($N = 7$, **R1**) and ($N = 7$, **R2**), which allow a qualitative description of the polydisperse medium, and ($N = 10$, **R3**), which provides a detailed description of the polydisperse bubble flow.

The discretized BSDs for the characteristic bubble size $d_b = 0.25$ mm are shown in Figure 2, with the exception of the monodisperse one, since it is elementary. It is worth noting some features of these distributions.

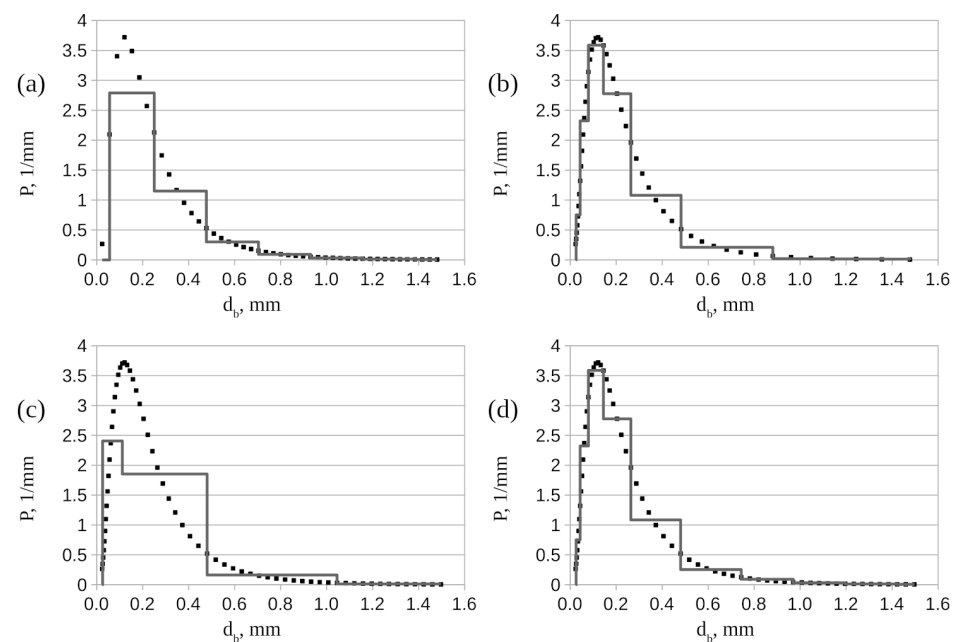


Figure 2. BSD function and piecewise approximations. The characteristic bubble size is $d_b = 0.25$ mm. (a) $N = 7$, **R1**; (b) $N = 7$, **R2**; (c) $N = 4$, **R3**; (d) $N = 10$, **R3**.

It can be seen that the distribution ($N = 7$, **R1**) does not describe the features of the distribution of small bubbles, providing for this domain only one class for bubbles from 0 to 0.25 mm. The distribution ($N = 7$, **R2**) resolves small bubbles at the expense of details for large bubbles. The distribution ($N = 4$, **R3**), despite some roughness, singles out a class for small and medium bubbles. The distribution ($N = 10$, **R3**) is the most detailed, describing both small and large bubbles well over the entire range.

4. Results and Discussion

4.1. Algorithm Verification

To assess the convergence of the algorithm by the number of classes N , the following parameters are used: the interfacial area S_{int} , the bubble volume fraction α_b , the bubble velocity V_b and the liquid velocity V_l . The bubble volume fraction, interfacial area and bubble velocity are calculated as follows:

$$\begin{aligned}\alpha_b &= \sum_{i=1}^N \alpha_{ib}, \\ S_{int} &= \sum_{i=1}^N n_{ib} \cdot \pi d_{ib}^2, \\ V_b &= \sum_{i=1}^N (\alpha_{ib} V_{ib}) / \alpha_b.\end{aligned}\quad (22)$$

The overall averaged values are used to monitor the convergence to a stable solution as N increases, as well as the deviation of solutions with number of classes N and $N-1$.

Figure 3 shows the averaged values of the variables mentioned above and the normalized deviation of the variable values compared to the solution obtained for $N-1$ bubble classes as a function of the number of classes. Due to the averaging procedure, these values represent the entire flow behavior. Figure 3 shows the averaged values of the above variables as a function of the number of classes and the normalized deviation of the variable values compared to the solution obtained for $N-1$ bubble classes. Due to the averaging procedure, the values represent the entire flow behavior.

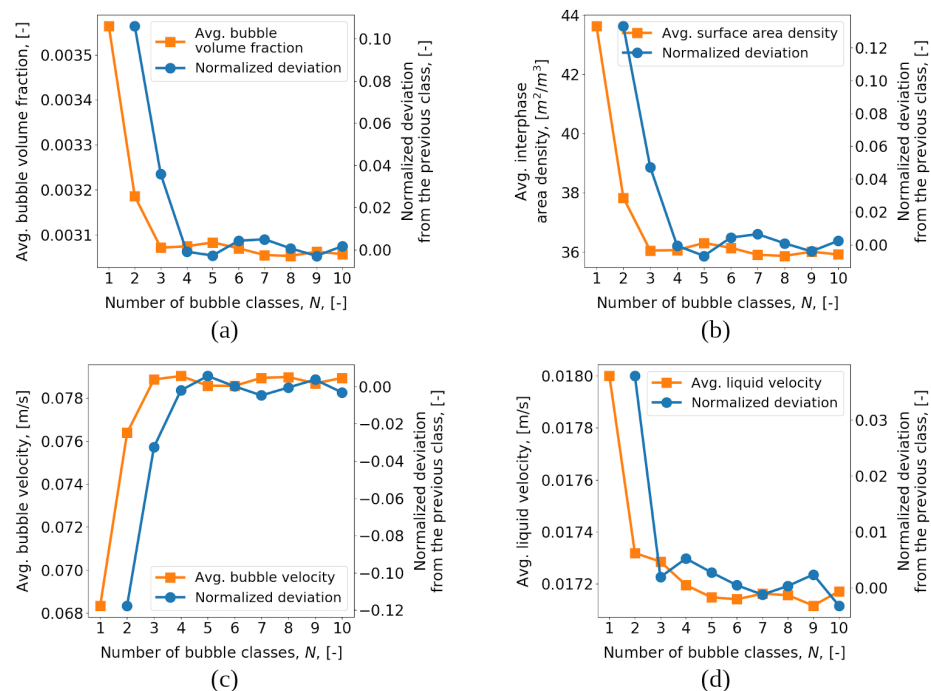


Figure 3. Distributions of flow parameters as a function of the number of bubble classes. The characteristic bubble size $d_b = 0.25$ mm; (a) the bubble volume fraction; (b) the interfacial area density; (c) the bubble velocity; (d) the liquid velocity.

It can be seen that the monodisperse approach overpredicts the total gas holdup within a column as well as the interfacial density. With increasing N the solution tends to converge to the polydisperse solution, with normalized deviation tending to the vicinity of zero at $N \geq 5$ for the bubble volume fraction, the interfacial area density and the bubble velocity. The differences between the variants are less than 1% at $N = 4$, indicating that sufficient detail is captured to estimate the integral flow parameters. However, the fluid velocity, despite having the lowest normalized deviation, also has the lowest rate of deviation decay, approaching 0 at $N > 6$. Thus, a converged solution in terms of N can be obtained at $N = 7$.

4.2. An Impact of Characteristic Bubble Size and Parameters of Approximation of the BSD Function on the Flow Structure

Some results of the BCR flow simulation are presented below. The radial profiles of the bubble volume fraction α_b (Figure 4), the interfacial surface area S_{int} (Figure 5), the bubble velocity V_b (Figure 6) and the carrier phase velocity V_l (Figure 7) are shown.

The data correspond to the reference cross-section (see Figure 1) for three characteristic bubble sizes (0.25 mm, 0.5 mm and 1 mm) and four variants of approximations: ($N = 1$, R1), ($N = 4$, R3), ($N = 7$, R1) and ($N = 10$, R3).

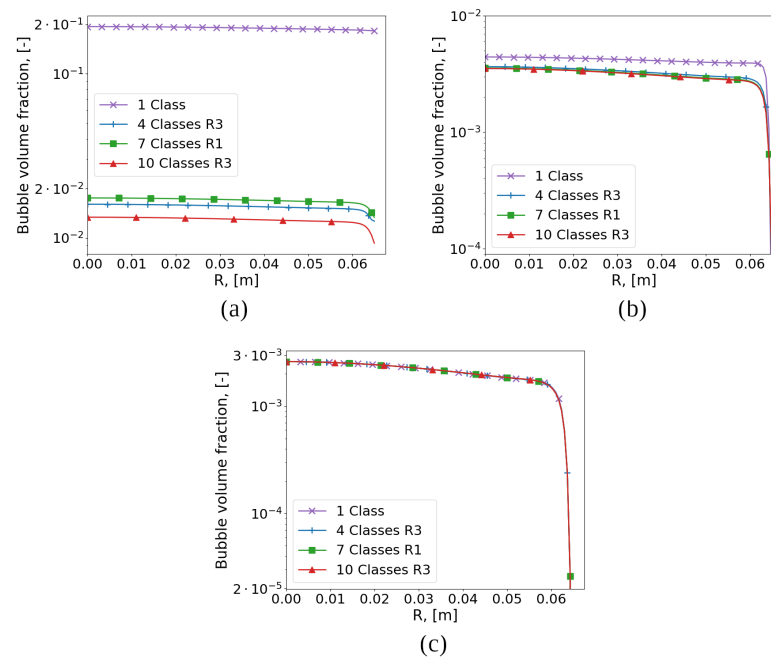


Figure 4. Radial profiles of the bubble volume fraction in the reference cross-section (see Figure 1) per different characteristic bubble sizes: (a) $M = 0.25$ mm; (b) $M = 0.5$ mm; (c) $M = 1.0$ mm.

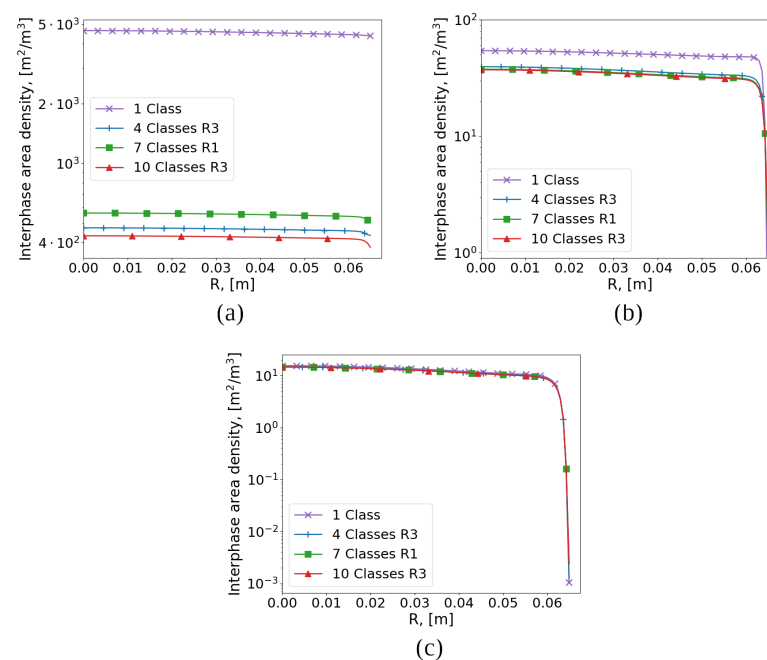


Figure 5. Radial profiles of the interfacial area density in the reference cross-section (see Figure 1) for different characteristic bubble sizes: (a) $M = 0.25$ mm; (b) $M = 0.5$ mm; (c) $M = 1.0$ mm.

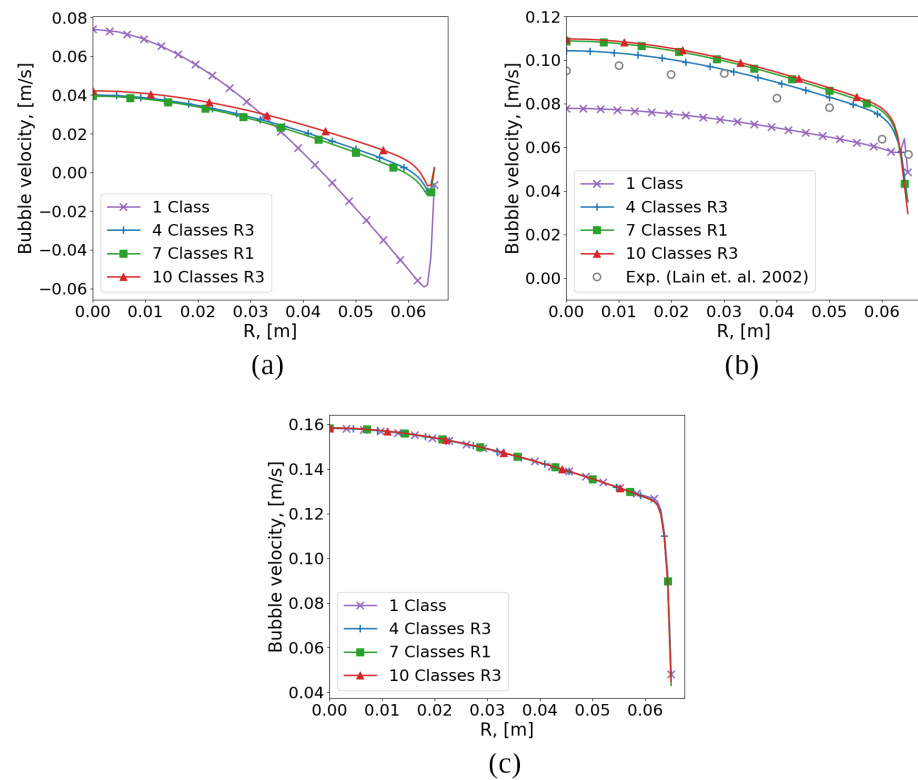


Figure 6. Radial profiles of bubble velocity in the reference cross-section (see Figure 1) for different characteristic bubble sizes: (a) $M = 0.25$ mm; (b) $M = 0.5$ mm; (c) $M = 1.0$ mm.

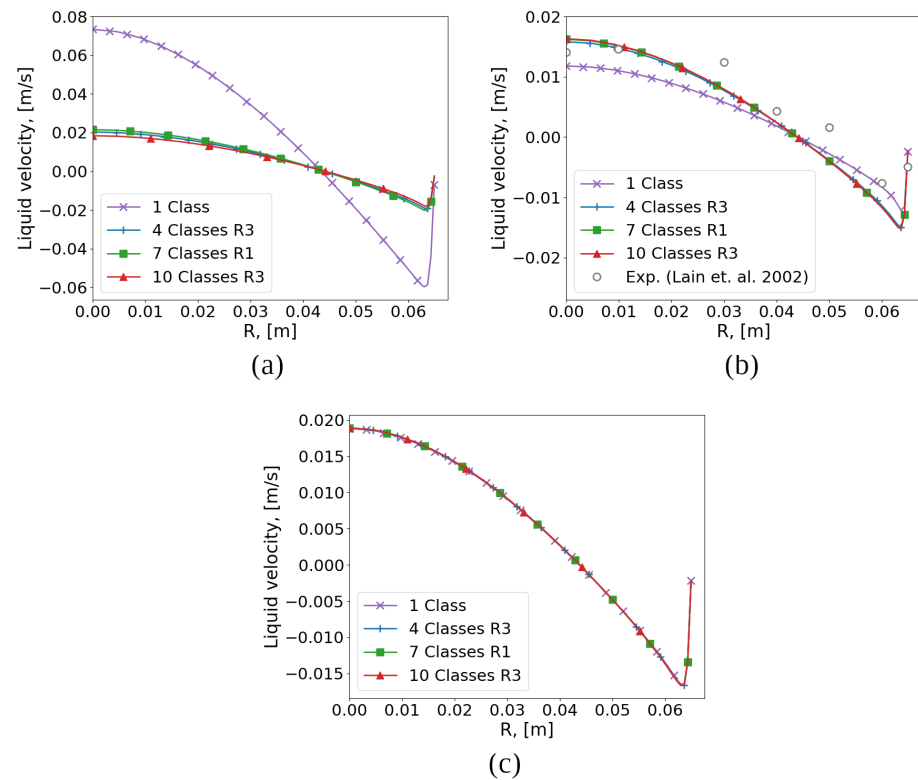


Figure 7. Radial profiles of liquid velocity in the reference cross-section (see Figure 1) for different characteristic bubble sizes: (a) $M = 0.25$ mm; (b) $M = 0.5$ mm; (c) $M = 1.0$ mm.

It can be seen that for small bubbles ($d_b = 0.25$ mm) there is a significant difference between the monodisperse and polydisperse approaches in all studied parameters. As the bubble size increases ($d_b = 1.00$ mm), the profiles of the volume fraction and the velocity of the carrier phase coincide for the two approaches. It should also be noted that, although the variant ($N = 4$, **R3**) has fewer bubble classes than ($N = 7$, **R1**), it gives a solution close to ($N = 10$, **R3**) for the volume fraction and the interfacial area, in contrast to ($N = 7$, **R1**). A comparison with the experimental data [22] for $d_b = 0.5$ mm shows that the option ($N = 4$, **R3**) is preferable.

The main emphasis is placed on the comparison of the obtained solutions with the “reference” solution for the case ($N = 10$, **R3**) as the most detailed representation of the BSD function. The comparison was carried out using the normalized variance of the obtained solution and the “reference” solution in the entire domain for a set of characteristic values of the polydisperse flow, such as the velocities of the carrier and dispersed phases, the volume fraction of the bubbles, and the interfacial area. The normalized variance was estimated according to the formula:

$$\sigma_{norm}(\phi) = \sqrt{\left[\sum_{i=1}^{N_{cells}} (\phi_i - \phi_i^*)^2 / N_{cells} \right] / \max(|\phi^*|)}, \quad (23)$$

where ϕ is the comparable variable for the solution under study and ϕ^* is the same variable in the same cell for the “reference” solution.

Below are plots of the weighted variances, σ_{norm} , as a function of case number and bubble diameter, d_b . For the case numbers, 1 stands for ($N = 1$, **R1**), 2 stands for ($N = 4$, **R3**), 3 stands for ($N = 7$, **R1**) and 4 stands for ($N = 7$, **R2**) (Figures 8–11).

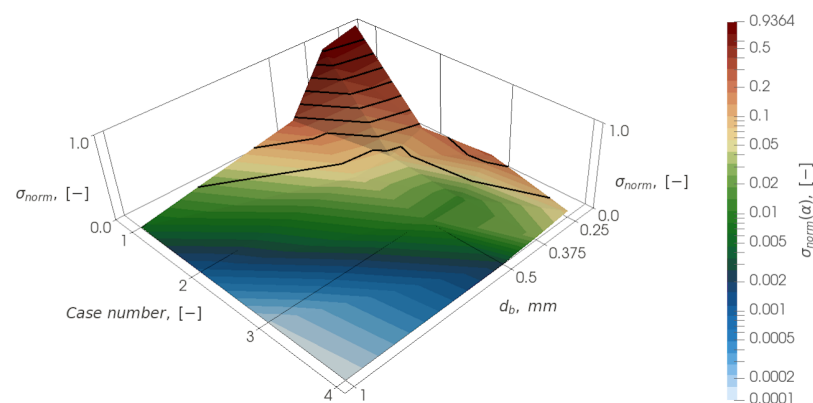


Figure 8. Distribution of a weighted variance σ_{norm} for the bubble volume fraction, α_b .

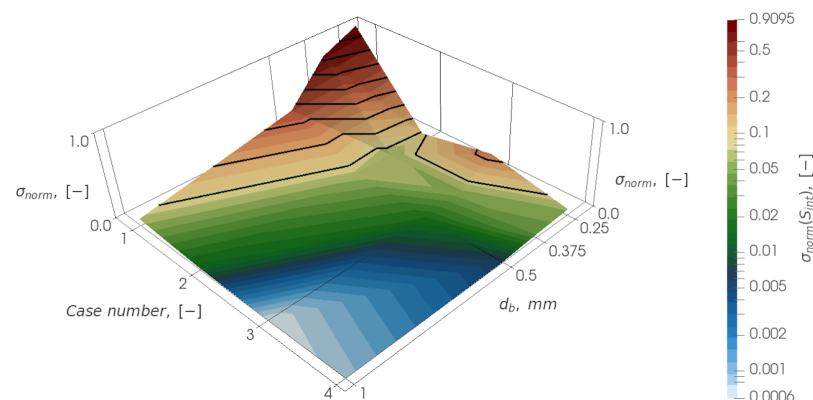


Figure 9. Distribution of a weighted variance σ_{norm} for the interfacial area density, S_{int} .

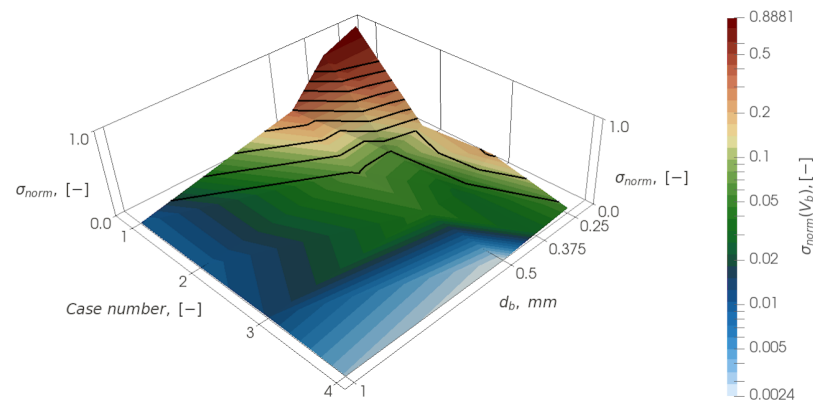


Figure 10. Distribution of a weighted variance σ_{norm} for the bubble velocity, V_b .

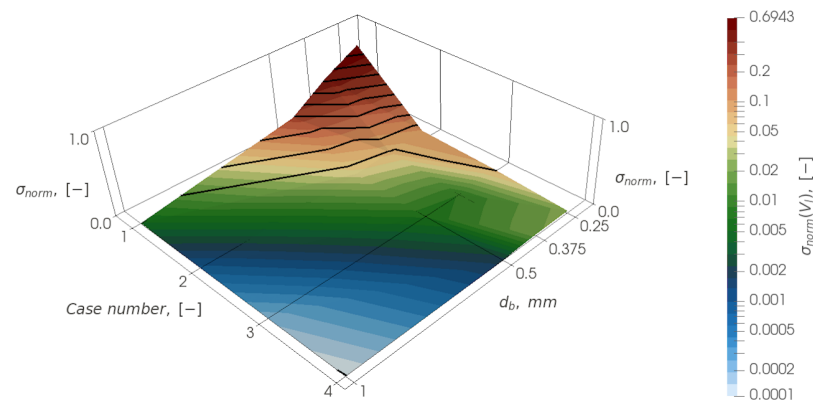


Figure 11. Distribution of a weighted variance σ_{norm} for the liquid velocity, V_l .

Based on the analysis of all four distributions, a general conclusion can be drawn: as the characteristic size of the bubbles increases, the difference between all approaches is leveled and, even for the monodisperse approach, the difference with the reference one turns out to be small: it is 5% for the interfacial area and about 1% for other quantities for a bubble diameter of 1 mm. However, for a bubble diameter of 0.5 mm, the difference between the monodisperse and polydisperse approaches becomes significant (up to 20%). The difference increases with decreasing bubble diameter.

For 0.5 mm bubbles the normalized variance decreases monotonically and the solution approaches the reference one with increase of N (variation of the parameters of the BSD function approximation): from monodisperse ($N = 1$, **R1**), then through distributions ($N = 4$, **R3**), ($N = 7$, **R1**) and ending with ($N = 7$, **R2**).

However, for the smallest bubble considered, with a diameter of 0.25 mm, this behavior changes. Using the distribution ($N = 4$, **R3**), a solution can be obtained that is close to the variant ($N = 7$, **R2**) and has a smaller difference from the “reference” one than ($N = 7$, **R1**). This can be explained by the fact that, in the case of the distribution ($N = 7$, **R1**), small bubbles corresponding to the left side of the BSD function are not resolved at all in the simulation. However, their influence is important since they have the ability to accumulate in stagnation or recirculation zones, significantly influencing the flow parameters and changing the flow structure. Although the distribution ($N = 4$, **R3**) is coarser than ($N = 7$, **R1**), it still describes the behavior of small bubbles.

5. Conclusions

The numerical simulation of the dynamics of polydisperse and monodisperse flows in the BCR was performed to clarify the effect of the parameters of the piecewise constant approximation of the BSD function.

It was found that with increasing of bubble size the normalized variances of the bubble volume fraction, the liquid velocity, and the specific density of the interfacial surface calculated for the polydisperse and monodisperse descriptions of the BCR working medium decrease. In particular, for bubbles with a characteristic size of $M = 1.0$ mm, the normalized variance is about 1% for the velocity and 5% for the density of the interfacial surface.

The discrete approximation of the BSD function with the uniform distribution of bins with respect to $\ln(d_b)$ (**R2**) provides a better solution, in terms of normalized variances, than that with the uniform bins with respect to d_b (**R1**), due to the correct resolution of the domain of small bubbles (with $d_b < M$).

A hybrid approximation of the BSD function **R3** has been proposed which is uniform with respect to $\ln(d_b)$ for bubbles with sizes smaller than M and uniform with respect to d_b for sizes larger than M . Such an approximation is potentially preferable with substantially large bubble sizes up to ($d_b > 6$ mm).

The hybrid approximation of the BSD (**R3**) with four classes of bubbles provides better results than the original **R1** approximation with seven classes and is comparable to the **R2** approximation with seven classes of bubbles. The obtained results were compared with the results for the **R3** approximation with 10 classes of bubbles as well as with the experimental data, and demonstrated qualitative and quantitative agreement. This makes the proposed approach promising for flow pattern prediction and robust due to low computational resource requirements.

Author Contributions: Conceptualization, A.C. and A.S.; methodology, A.C. and A.S.; software, A.C.; validation, A.C. and V.C.; formal analysis, A.S.; investigation, A.S.; writing—original draft preparation, A.C., A.S. and V.C.; writing—review and editing, A.C. and A.S.; visualization, A.C. and V.C.; supervision, A.S.; project administration, A.S.; funding acquisition, A.S. All authors have read and agreed to the published version of the manuscript.

Funding: This research received no external funding.

Institutional Review Board Statement: Not applicable.

Informed Consent Statement: Not applicable.

Data Availability Statement: Data available upon request.

Conflicts of Interest: The authors declare no conflict of interest.

Abbreviations

The following abbreviations are used in this manuscript:

BCR	Bubble column reactor
BSD	Bubble size distribution
MUSIG	Multiple size group
TVD	Total variation diminishing
SIMPLE	Semi-implicit method for pressure-linked equations

References

1. Yang, X.; Liu, Z.; Manhaeghe, D.; Yang, Y.; Hogue, J.; Demeestere, K.; van Hulle, S.W.H. Intensified ozonation in packed bubble columns for water treatment: Focus on mass transfer and humic acids removal. *Chemosphere* **2021**, *283*, 131217. [[CrossRef](#)] [[PubMed](#)]
2. Inkeri, E.; Tynjälä, T. Modeling of CO₂ Capture with Water Bubble Column Reactor. *Energies* **2020**, *13*, 5793. [[CrossRef](#)]
3. Perez, B.J.L.; Jimenez, J.A.M.; Bhardwaj, R.; Goetheer, E.; van Sint Annaland, M.; Gallucci, F. Methane pyrolysis in a molten gallium bubble column reactor for sustainable hydrogen production: Proof of concept & techno-economic assessment. *Int. J. Hydrogen Energy* **2021**, *46*, 4917–4935. [[CrossRef](#)]
4. Vik, C.B.; Solsvik, J.; Hillestad, M.; Jakobsen, H.A. Interfacial mass transfer limitations of the Fischer-Tropsch synthesis operated in a slurry bubble column reactor at industrial conditions. *Chem. Eng. Sci.* **2018**, *192*, 1138–1156. [[CrossRef](#)]
5. Kantarci, N.; Borak, F.; Ulgen, K.O. Bubble column reactors. *Process Biochem.* **2005**, *40*, 2263–2283. [[CrossRef](#)]
6. Lau, Y.M.; Thiruvalluvan Sujatha, K.; Gaeini, M.; Deen, N.G.; Kuipers, J.A.M. Experimental study of the bubble size distribution in a pseudo-2D bubble column. *Chem. Eng. Sci.* **2013**, *98*, 203–211. [[CrossRef](#)]

7. Besagni, G.; Inzoli, F. Prediction of Bubble Size Distributions in Large-Scale Bubble Columns Using a Population Balance Model. *Computations* **2019**, *7*, 17. [\[CrossRef\]](#)
8. Pakhomov, M.A.; Terekhov, V.I. Simulation of the turbulent structure of a flow and heat transfer in an ascending polydisperse bubble flow. *Tech. Phys.* **2015**, *60*, 1268–1276. [\[CrossRef\]](#)
9. Yao, W.; Morel, C. Volumetric interfacial area prediction in upward bubbly two-phase flow. *Int. J. Heat Mass Transf.* **2004**, *47*, 307–328. [\[CrossRef\]](#)
10. Wang, T.; Wang, J.; Jin, Y. Population Balance Model for Gas-Liquid Flows: Influence of Bubble Coalescence and Breakup Models. *Ind. Eng. Chem. Res.* **2005**, *44*, 7540–7549. [\[CrossRef\]](#)
11. Lo, S. *Application of Population Balance to CFD Modelling of Bubbly Flow via the MUSIG Model*; AEA Technology: Rotherham, UK, 1996.
12. Krepper, E.; Lucas, D.; Frank, T.; Prasser, H.-M.; Zwart, P.J. The inhomogeneous MUSIG model for the simulation of polydispersed flows. *Nucl. Eng. Des.* **2008**, *238*, 1690–1702. [\[CrossRef\]](#)
13. Ziegenhein, T.; Rzehak, R.; Lucas, D. Transient simulation for large scale flow in bubble columns. *Chem. Eng. Sci.* **2015**, *122*, 1–13. [\[CrossRef\]](#)
14. Olmos, E.; Gentric, C.; Vial, C.; Wild, G.; Midoux, N. Numerical simulation of multiphase flow in bubble column reactors. Influence of bubble coalescence and break-up. *Chem. Eng. Sci.* **2001**, *56*, 6359–6365. [\[CrossRef\]](#)
15. Fard, M.G.; Stiriba, Y.; Gourich, B.; Vial, C.; Grau, F.X. Euler–Euler large eddy simulations of the gas–liquid flow in a cylindrical bubble column. *Nucl. Eng. Des.* **2020**, *369*, 110823. [\[CrossRef\]](#)
16. Zhang, X.B.; Yan, W.C.; Luo, Z.H. Numerical simulation of local bubble size distribution in bubble columns operated at heterogeneous regime. *Chem. Eng. Sci.* **2021**, *231*, 116266. [\[CrossRef\]](#)
17. Wu, Y.; Liu, Z.; Li, B.; Gan, Y. Numerical simulation of multi-size bubbly flow in a continuous casting mold using population balance model. *Powder Technol.* **2022**, *396*, 224–240. [\[CrossRef\]](#)
18. Wu, Y.; Liu, Z.; Li, B.; Xiao, L.; Gan, Y. Numerical simulation of multi-size bubbly flow in a continuous casting mold using an inhomogeneous multiple size group model. *Powder Technol.* **2022**, *402*, 117368. [\[CrossRef\]](#)
19. Bhole, M.R.; Joshi, J.B.; Ramkrishna, D. CFD simulation of bubble columns incorporating population balance modeling. *Chem. Eng. Sci.* **2008**, *63*, 2267–2282. [\[CrossRef\]](#)
20. Chernyshev, A.S.; Schmidt, A.A. Investigation of the evolution of the bubble size distribution in the ascending and descending flows. *J. Phys. Conf. Ser.* **2017**, *899*, 032009. [\[CrossRef\]](#)
21. Lain, S.; Broder, D.; Sommerfeld, M. Experimental and numerical studies of the hydrodynamics in a bubble column. *Chem. Eng. Sci.* **1999**, *54*, 4913–4920. [\[CrossRef\]](#)
22. Lain, S.; Broder, D.; Sommerfeld, M.; Goz, M.F. Modelling hydrodynamics and turbulence in a bubble column using the Euler–Lagrange procedure. *Int. J. Multiph. Flow* **2002**, *28*, 1381–1407. [\[CrossRef\]](#)
23. Roghair, I.; Lau, Y.M.; Deen, N.G.; Slagter, H.M.; Baltussen, M.W.; van Sint Annaland, M.; Kuipers, J.A.M. On the drag force of bubbles in bubble swarms at intermediate and high Reynolds numbers. *Chem. Eng. Sci.* **2011**, *66*, 3204–3211. [\[CrossRef\]](#)
24. Auton, T.R. The lift force on a spherical body in a rotational flow. *J. Fluid Mech.* **1987**, *183*, 199–218. [\[CrossRef\]](#)
25. Tomiyama, A.; Tamai, H.; Zun, I.; Hosokawa, S. Transverse migration of single bubbles in simple shear flows. *Chem. Eng. Sci.* **2002**, *57*, 1849–1858. [\[CrossRef\]](#)
26. Menter, F.R.; Kuntz, M.; Langtry, R. Ten Year of Industrial Experience with the SST Turbulence Model. In Proceedings of the 4th International Symposium on Turbulence, Heat and Mass Transfer, Antalya, Turkey, 12–17 October 2003; pp. 625–632.
27. Troshko, A.A.; Hassan, Y.A. A two-equation turbulence model of turbulent bubbly flows. *Int. J. Multiph. Flow* **2001**, *27*, 1965–2000. [\[CrossRef\]](#)
28. Sato, Y.; Sekoguchi, R. Liquid velocity distribution in two-phase bubble flow. *Int. J. Multiph. Flow* **1975**, *2*, 79–95. [\[CrossRef\]](#)
29. Sokolichin, A.; Eigenberger, G.; Lapin, A. Simulation of Buoyancy Driven Bubbly Flow: Established Simplifications and Open Questions. *AIChE J.* **2004**, *50*, 24–45. [\[CrossRef\]](#)
30. Moraga, F.J.; Larreteguy, A.E.; Drew, D.A.; Lahey, R.T., Jr. Assessment of turbulent dispersion models for bubbly flows in the low Stokes number limit. *Int. J. Multiph. Flow* **2003**, *29*, 655–673. [\[CrossRef\]](#)
31. Versteeg, H.K.; Malalasekera, W. *An Introduction to Computational Fluid Dynamics. The Finite Volume Method*, 2nd ed.; Pearson Education Limited: Harlow, UK, 2007; pp. 134–211.
32. Chernyshev, A.S.; Schmidt, A.A. Numerical modeling of gravity-driven bubble flows with account of polydispersion. *J. Phys. Conf. Ser.* **2016**, *754*, 032005. [\[CrossRef\]](#)
33. Chernyshev, A.S.; Schmidt, A.A. Numerical simulation of gravity-driven mono- and polydisperse bubbly flows in a three-dimensional column in the framework of the Euler–Euler approach. *J. Phys. Conf. Ser.* **2020**, *1697*, 012236. [\[CrossRef\]](#)
34. Chen, P.; Sanyal, J.; Dudukovic, M.P. Numerical simulation of bubble columns flows: Effect of different breakup and coalescence closures. *Chem. Eng. Sci.* **2005**, *60*, 1085–1101. [\[CrossRef\]](#)
35. Allio, A.; Buffo, A.; Marchisio, D.; Savoldi, L. Two-fluid modelling for poly-disperse bubbly flows in vertical pipes: Analysis of the impact of geometrical parameters and heat transfer. *Nucl. Eng. Technol.* **2022**, *in press*. [\[CrossRef\]](#)

Disclaimer/Publisher’s Note: The statements, opinions and data contained in all publications are solely those of the individual author(s) and contributor(s) and not of MDPI and/or the editor(s). MDPI and/or the editor(s) disclaim responsibility for any injury to people or property resulting from any ideas, methods, instructions or products referred to in the content.